

# Porous media gravity current flow over an interbed layer: the impact of dispersion and distributed drainage

S. Sheikhi<sup>1,†</sup> and M.R. Flynn<sup>1</sup>

<sup>1</sup>Department of Mechanical Engineering, University of Alberta, Edmonton, Canada T6G 1H9

(Received 6 October 2023; revised 13 January 2024; accepted 23 February 2024)

---

Motivated by buoyancy-driven flows within geological formations, we study the evolution of a (dense) gravity current in a porous medium bisected by a thin interbed layer. The gravity current experiences distributed drainage along this low-permeability boundary. Our theoretical description of this flow takes into account dispersive mass exchange with the surrounding ambient fluid by considering the evolution of the bulk and dispersed phases of the gravity current. In turn, we model basal draining by considering two bookend limits, i.e. no mixing versus perfect mixing in the lower layer. Our formulations are assessed by comparing model predictions against the output of complementary numerical simulations run using COMSOL. Numerical output is essential both for determining the value of the entrainment coefficient used within our theory and for assessing the reasonableness of key modelling assumptions. Our results suggest that the degree of dispersion depends on the dip angle and the depth and permeability of the interbed layer. We further find that the nose position predictions made by our theoretical models are reasonably accurate up to the point where the no mixing model predicts a retraction of the gravity current front. Thereafter, the no mixing model significantly under-predicts, and the perfect mixing model moderately over-predicts, numerical data. Reasons for the failure of the no mixing model are provided, highlighting the importance of convective instabilities in the lower layer. A regime diagram is presented that defines the parametric region where our theoretical models do versus do not yield predictions in good agreement with numerical simulations.

**Key words:** gravity currents, porous media, dispersion

---

† Email address for correspondence: [sheikhim@ualberta.ca](mailto:sheikhim@ualberta.ca)

## 1. Introduction

In layered porous media, the flow of a dense (buoyant) fluid into a buoyant (dense) ambient leads to the formation of gravity currents, where predominantly the flow velocity is aligned with the bottom (top) boundary. Porous media gravity currents are associated with a wide variety of geophysical flows, whether naturally occurring, e.g. seawater contamination of coastal aquifers (Werner *et al.* 2013; Costall *et al.* 2020), or else related to human activities, e.g. underground hydrogen storage (UHS) (Feldmann *et al.* 2016; Tarkowski 2019; Muhammed *et al.* 2023) or CO<sub>2</sub>/acid gas sequestration (Ajayi, Gomes & Bera 2019; Warnecki *et al.* 2021; Ali *et al.* 2022). Not surprisingly, a significant volume of research has been driven by the need to understand the dynamics of porous media gravity currents, particularly as they relate to energy industry applications.

In a pioneering study, Huppert & Woods (1995) established initial models for porous media gravity current flow. They proposed a similarity solution that was then verified through laboratory experiments. Huppert & Woods (1995) showed that a gravity current spreads as  $t^{2/3}$  when fed by a constant-flux source. (Separately, they also derived similarity solutions for a general power-law influx condition.) Many extensions to the Huppert & Woods (1995) seminal analysis have been pursued. For example, Hesse *et al.* (2007), MacMinn *et al.* (2012), Pegler, Huppert & Neufeld (2014) and Zheng *et al.* (2015) have examined similar examples of buoyancy-driven flow but in porous media that are confined vertically. A question of recent interest, which is more relevant to the research described in this study, is the impact of a heterogeneous porous medium, particularly when some fraction of the injectate is allowed to drain through local or distributed fissures. For example, Anderson, McLaughlin & Miller (2003) investigated the movement of gravity currents in strongly heterogeneous porous media using homogenization methods. They found that by employing appropriate coefficients, one can project the similarity solution appropriate for a (long and thin) gravity current in a uniform medium to gravity current flow in horizontally or vertically layered porous media. Moreover, Pritchard, Woods & Hogg (2001) and Farcas & Woods (2009) studied distributed drainage over a thin permeable layer. The Pritchard *et al.* (2001) investigation considered miscible flow with drainage along a horizontal layer while Farcas & Woods (2009) studied immiscible flow with drainage along an inclined layer. Meanwhile, Neufeld & Huppert (2009) studied the flow of gravity currents of supercritical CO<sub>2</sub> in thin layers representing the Utsira formation beneath the North Sea. In contrast to the modelling approach of Pritchard *et al.* (2001), who did not consider the possible dynamical influence of the drained fluid on the evolution of the gravity current, Neufeld & Huppert (2009) hypothesized that when gravity current fluid drains into the interbed layers that separate adjacent permeable layers, such an influence is manifest. More precisely, the weight of the drained fluid adds to the driving force for draining so that, over time, the velocities of drainage and of the gravity current front become respectively large and small. Neufeld & Huppert (2009) thereby identified three distinct regimes for the drainage of (dense) gravity current fluid, i.e. drainage is driven primarily by (i) the weight of the gravity current, (ii) the combined weight of the gravity current and the fluid already drained into the lower layer, and (iii) the weight of the drained fluid. Regimes (ii) and (iii) are respectively associated with the arrest and retraction of the gravity current front. Similar kinds of flow behaviour have been documented in the related studies of Goda & Sato (2011), Acton, Huppert & Worster (2001), Sahu & Flynn (2017) and Bharath, Sahu & Flynn (2020), who examined, theoretically and experimentally, distributed drainage over a deep lower layer having a relatively small permeability. Most notably, and consistent with Pritchard *et al.* (2001) and Farcas & Woods (2009), these related studies found that gravity currents stop elongating

when the rate of basal drainage from the gravity current underside matches the source influx.

Most of the above research ignores mass transfer between the gravity current and the ambient fluid saturating the porous medium, e.g. by application of a ‘sharp interface’ assumption in theoretical models. By contrast, and in the context of CO<sub>2</sub> sequestration, Neufeld *et al.* (2010), MacMinn *et al.* (2012), Pegler *et al.* (2014) and Khan, Bharath & Flynn (2022) investigated mixing due to convective dissolution in porous media buoyancy-driven flow. Also, mass transfer processes associated with seawater intrusions into coastal aquifers were considered by Huyakorn *et al.* (1987) and Paster & Dagan (2007). In such examples of miscible porous media flow, the key modes of mass transfer are diffusion and hydrodynamic dispersion. Mixing by dispersion is likewise important when considering the societally important possibility of storing hydrogen (H<sub>2</sub>) in depleted natural gas reservoirs. Indeed, the combination of H<sub>2</sub> leakage through cap-rock and the dispersive mixing of H<sub>2</sub> into the ‘cushion gas’ that otherwise occupies the porous medium reduces the volume of H<sub>2</sub> that can be recovered economically. Quantifying such details is challenging; e.g. the study by Lubon & Tarkowski (2021) estimated the amount of recoverable H<sub>2</sub> as anywhere from 50 % to 80 % depending on, among other factors, the number of H<sub>2</sub> injection cycles and the degree of heterogeneity within the medium. As regards this latter variable, Feldmann *et al.* (2016) highlighted the possibility of leakage through semi-permeable boundaries by examining H<sub>2</sub> migration through a heterogeneous porous medium consisting of sandstone layers separated by tight clay interlayers.

Also in the context of miscibility, Szulczewski & Juanes (2013) studied, theoretically, mixing when a fixed amount of dense fluid is released in vertically confined porous media. They reported evidence of various regimes associated with the flow evolution. At early and more especially late times, diffusion is vital, especially when it is coupled with Taylor dispersion. However, at intermediate times, diffusion is insignificant, such that application of the sharp interface assumption is approximately correct. Meanwhile, Sahu & Neufeld (2020) studied, theoretically and experimentally, the mixing that occurs in a homogeneous porous medium due to velocity-dependant transverse dispersion in gravity currents. In their theoretical model, they exploited mass and buoyancy conservation laws in conjunction with a semi-empirical expression for dispersion, analogue to turbulent entrainment in free shear flows. Sahu & Neufeld (2020) tuned the associated entrainment coefficient from their theoretical model with measured results from the laboratory. Although transverse dispersion leads, through ‘dispersive entrainment’, to a thickening of the gravity current, the neglect of longitudinal dispersion means that the gravity current length predicted by Sahu & Neufeld (2020) must match that anticipated by the sharp interface model of Huppert & Woods (1995).

The equivalence documented at the end of the previous paragraph runs contrary to the experimental observations of Bharath *et al.* (2020). They studied gravity currents propagating along a permeability jump, and demonstrated that dispersion leads to enhanced gravity current elongation. The difference of length compared to the sharp interface case was attributed to longitudinal dispersion. The Sahu & Neufeld (2020) model therefore appears most effective in describing gravity current flow through homogeneous media where drainage is not dynamically significant. Recognizing that real geological media are not always so ideal, Sahu & Neufeld (2023) conducted laboratory experiments to examine dispersive mixing in gravity currents over layered strata. They showed that the mixing that occurs in heterogeneous media is approximately twice that in homogeneous media having otherwise identical properties. To quantify the effects of heterogeneity

on mixing, Sahu & Neufeld (2023) introduced a term called the ‘jump factor’, which characterizes the degree of layering within a porous medium. Sahu & Neufeld (2023) further demonstrated that the early-time entrainment into the gravity current renders it thick with a rounded nose. Therefore, the long and thin assumption, which is vital in developing a theoretical model, becomes suspect. Sahu & Neufeld (2023) used their experimental findings to derive semi-empirical equations that estimate the gravity current height and length as functions of time and other parameters. The semi-empirical correlations in question do not, however, distinguish between bulk and dispersed phases within the gravity current. A pioneering theoretical attempt at drawing such a distinction was made by Sahu & Neufeld (2020), whose approach was later expanded upon by Sheikhi, Sahu & Flynn (2023). The authors of this latter investigation separated the bulk and dispersed phases to study dispersive mixing in gravity currents elongating over inclined porous media and experiencing local drainage through discrete fissures. Sheikhi *et al.* (2023) thereby extended the theoretical model of Sahu & Neufeld (2020) by introducing two entrainment velocities, i.e.  $w_{e1}$ , which is associated with entrainment from the bulk phase to the dispersed phase, and  $w_{e2}$ , which is associated with entrainment from the surrounding ambient to the dispersed phase. They assumed an identical entrainment coefficient associated with  $w_{e1}$  and  $w_{e2}$ , and determined the numerical value of this entrainment coefficient by fitting theoretical predictions against COMSOL-based numerical simulations meant to mimic similitude laboratory experimental conditions. Their theoretical model, combined with the COMSOL numerical simulations, revealed that five parameters can affect the amount of dispersive mixing in porous media gravity currents experiencing local drainage: (i)  $\Gamma$ , which represents flow conditions upstream of the local fissure(s); (ii)  $K$ , which represents the permeability ratio (fissure-to-medium); (iii)  $\xi$ , which represents the fissure width; (iv)  $l$ , which represents the fissure depth; and (v)  $\theta$ , which represents the dip angle.

A primary objective of this study is to extend the work of Sheikhi *et al.* (2023) to gravity currents experiencing distributed drainage, as is more representative of many geological flows compared to the case of localized drainage. To do so, we suppose that the gravity current propagates through a porous medium and over a thin interbed layer having a lower – possibly substantially lower – permeability. We develop a theoretical model and a complementary numerical model to study the details of the dispersive mixing relevant to this case. In the former case, our formulation is predicated on two linearizations of the real behaviour. The first pertains to fluid mechanics and supposes a linear entrainment law of the type proposed for high-Reynolds-number shear flows by Ellison & Turner (1959) and for low-Reynolds-number porous media flows by Sahu & Neufeld (2020). The second pertains to thermodynamics and supposes a linear equation of state, i.e. a linear relationship between fluid density and solute concentration. The latter linearization in particular seems well-justified in a UHS context: measured data from Hassanpouryouzband *et al.* (2020) suggest that nonlinear terms in the equation of state describing  $H_2/CH_4$  mixtures have minor significance. Meanwhile, the validity of the former linearization is discussed in more detail below. A further objective of our study is to characterize the drainage of gravity current fluid into the interbed layer and, from there, into a semi-infinite layer of larger permeability below. (For analytical convenience and consistent with previous studies – e.g. Huppert & Woods (1995), Neufeld & Huppert (2009), Bharath *et al.* (2020) and Sahu & Neufeld (2023) – we assume a dense rather than a light gravity current. As a result, the gravity current appears ‘upside down’ relative to those expected e.g. in UHS-type flows. Note, however, that the flow orientation does not impact the flow dynamics provided that we apply the Boussinesq approximation, which

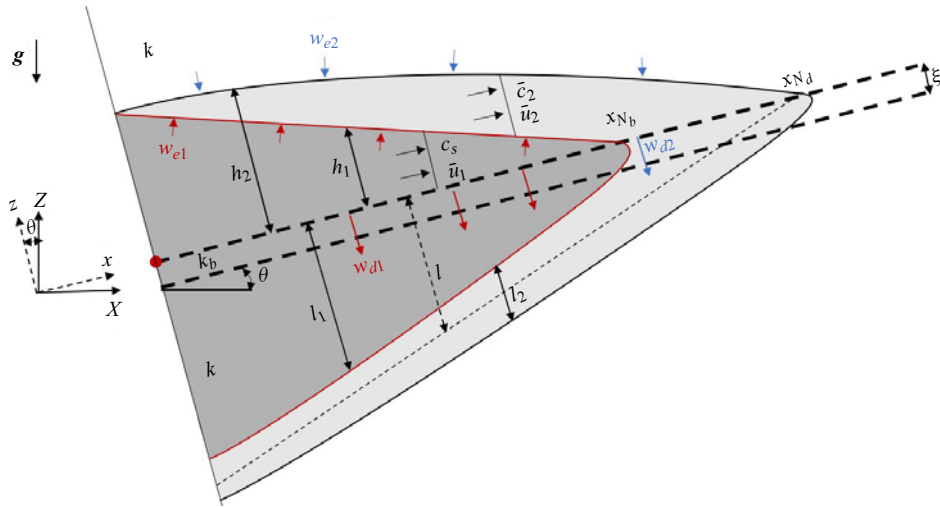


Figure 1. Schematic of a leaky gravity current propagating along, and draining through, the permeability jump associated with an interbed layer of thickness  $\xi$ . We assume equal permeability  $k$  in the upper and lower layers, and a reduced permeability  $k_b$  in the interbed layer. The gravity current and the fluid that drains from the gravity current consist of bulk and dispersed phases. These are, respectively, confined by the red and black curves. Meanwhile, the dashed curve that is drawn through the lower two layers signifies the equivalent depth of draining fluid, assuming that this draining fluid consists solely of bulk fluid, i.e. has a density that matches the source density. The variables  $h_1$ ,  $h_2$ ,  $u_1$ ,  $u_2$ ,  $w_{e1}$ ,  $w_{e2}$  and  $\bar{c}_2$  depend on  $x$  and  $\tilde{t}$ . Conversely, the variables  $x_{N_b}$  and  $x_{N_d}$  depend only on  $\tilde{t}$ . The vertical scale is exaggerated in this schematic.

supposes relatively modest density differences between the injectate and the ambient fluid.)

The rest of the paper is organized as follows. Section 2 derives the theoretical model for the gravity current by incorporating a distributed drainage formulation. Particular attention is paid to two limiting cases, which assume either no mixing or perfect mixing in the lowest of the porous layers. In § 3, we outline the COMSOL-based numerical simulations conducted to validate and contextualize the predictions of the theoretical model. In § 4, we discuss these predictions in more detail, and contrast the predictions with complementary output from the numerical simulations. Finally, key findings of the current work are reviewed, and prospects for future research are identified, in § 5.

## 2. Theoretical model

### 2.1. Governing equations

We examine the flow of a gravity current,  $z \geq 0$  in figure 1, that occurs when a dense fluid with density  $\rho_s$  is injected into a uniform porous medium with constant permeability  $k$ . This medium is intersected by a thin interbed layer of permeability  $k_b < k$  with inclination angle  $\theta$  and depth  $\xi$ . Thus the interbed layer occupies the vertical expanse  $-\xi < z < 0$ . In general, and with the application of (buoyant)  $H_2$  storage in an anticline structure in mind, we consider an up-dip inclination angle. The  $(x, z)$  coordinate system that describes the directions along and perpendicular to the slope is derived by rotating the natural coordinates  $(X, Z)$  in a clockwise direction by the dip angle  $\theta$ . The red dot shown in figure 1 signifies the isolated source, and the origin for both coordinate systems is located at this same point.

The continuity equation for the bulk (or unmixed) phase of the gravity current experiencing drainage over its lower boundary reads

$$\frac{\partial h_1}{\partial \tilde{t}} + \frac{\partial}{\partial x}(u_1 h_1) = -w_{e1} - w_{d1}. \tag{2.1}$$

Here,  $h_1$  is the height of the bulk phase,  $u_1$  is the bulk phase velocity, and  $w_{e1}$  and  $w_{d1}$  are velocities that respectively account for entrainment from the bulk to the dispersed phase and drainage from the bulk phase through the lower layer. Also,  $\tilde{t} = t/\phi$ , in which  $\phi$  is the porosity. (Note that all velocities in our theoretical model are Darcy velocities.)

Similarly, the continuity equation for the dispersed phase can be stated as

$$\frac{\partial h_2}{\partial \tilde{t}} + \frac{\partial}{\partial x}[u_2(h_2 - h_1)] = -\frac{\partial}{\partial x}(u_1 h_1) + w_{e2} - w_{d1} - w_{d2}, \tag{2.2}$$

where  $h_2 - h_1$  is the thickness of the dispersed phase,  $u_2$  (assumed independent of  $z$ ) is the advection speed of the dispersed phase,  $w_{e2}$  is the entrainment velocity from the ambient to the dispersed phase, and  $w_{d2}$  is the drainage velocity from the dispersed phase through the lower layer. The latter velocity must be interpreted with some care because it is not defined everywhere along the extent  $0 \leq x \leq x_{N_d}$  occupied by the dispersed phase (and likewise for  $w_{d1}$ ). We clarify this situation when formally defining the draining velocities  $w_{d1}$  and  $w_{d2}$  below.

Although the solute concentration in the bulk phase is equal to the source concentration  $c_s$  by assumption, the concentration in the dispersed phase varies between 0 and  $c_s$ . Therefore a  $z$ -averaged solute concentration  $\bar{c}_2$  is defined in the dispersed phase. Solute conservation in the dispersed phase can be expressed as

$$\frac{\partial b_2}{\partial \tilde{t}} + \frac{\partial}{\partial x}(u_2 b_2) = w_{e1} c_s H(x_{N_b} - x) - w_{d2} \bar{c}_2, \tag{2.3}$$

in which  $b_2 = \bar{c}_2(h_2 - h_1)$  is the buoyancy of the dispersed phase, averaged over depth. Meanwhile  $H(x_{N_b} - x)$  is a Heaviside step function, which is zero everywhere except when  $x_{N_b} > x$ , where  $x_{N_b}$  indicates the front position of the bulk phase. In this study, we follow previous work on entraining flows from either the turbulent free shear flow literature (e.g. Ellison & Turner 1959) or, much more importantly, the porous media flow literature (e.g. Sahu & Neufeld 2020), and so consider a linear entrainment relationship. Accordingly, the entrainment velocities are defined as  $w_{e1} = \varepsilon u_1$  and  $w_{e2} = \varepsilon u_2$ , where  $\varepsilon$  is the dispersive entrainment coefficient. Extrapolation of these relationships to more complicated formulations (e.g.  $w_{e1} = \varepsilon_1 u_1$  and  $w_{e2} = \varepsilon_2 u_2$  with  $\varepsilon_1 \neq \varepsilon_2$ , or  $w_{ei} \propto u_i^\lambda$  or  $w_{e1} \propto |u_1 - u_2|$ ) remains a topic to be examined in future studies. Our reluctance to pursue such a line of inquiry here stems not from the physical illogicality of these alternative formulations but rather from our desire to minimize model complexity and the number of variables whose value must be set by comparison with numerical output.

By considering a hydrostatic pressure gradient throughout the gravity current and using Darcy’s law, the horizontal velocity in each phase is given by

$$u_1(x, \tilde{t}) = -\frac{kg\beta}{\nu} \left[ \frac{\partial b_2}{\partial x} \cos \theta + c_s \left( \frac{\partial h_1}{\partial x} \cos \theta + \sin \theta \right) \right], \tag{2.4}$$

$$u_2(x, \tilde{t}) = -\frac{kg\beta}{\nu} \left[ \frac{\partial(\bar{c}_2 h_2)}{\partial x} \cos \theta + \bar{c}_2 \sin \theta \right] \equiv -\frac{kg\beta}{\nu} \left[ \frac{\partial}{\partial x} \left( \frac{b_2 h_2}{h_2 - h_1} \right) \cos \theta + \bar{c}_2 \sin \theta \right] \tag{2.5}$$

(see Sheikhi *et al.* 2023). Here,  $\beta$  is the solute contraction coefficient, which we borrow from the (assumed linear) equation of state  $\rho = \rho_0(1 + \beta c)$  in which  $\rho_0$  is the density of

the uncontaminated ambient fluid. Also,  $\nu$  is the kinematic viscosity, which we assume to be the same throughout the bulk and dispersed phases. By inserting (2.4)–(2.5) and the expressions for the entrainment velocities  $w_{e,1}$  and  $w_{e,2}$  into (2.1)–(2.3), we obtain the following modified governing equations:

$$\frac{\partial h_1}{\partial \tilde{t}} + \frac{kg'_s}{\nu} \frac{\partial(h_1 U)}{\partial x} = -\varepsilon \frac{kg'_s}{\nu} U - w_{d1}, \tag{2.6}$$

$$\begin{aligned} \frac{\partial h_2}{\partial \tilde{t}} - \frac{kg'_s}{\nu} \frac{\partial}{\partial x} \left[ (h_2 - h_1) \left( \frac{\partial \Psi}{\partial x} + C \sin \theta \right) - h_1 U \right] \\ = -\varepsilon \frac{kg'_s}{\nu} \left( \frac{\partial \Psi}{\partial x} + C \sin \theta \right) - w_{d1} - w_{d2}, \end{aligned} \tag{2.7}$$

$$\frac{\partial b_2}{\partial \tilde{t}} - \frac{kg'_s}{\nu} \frac{\partial}{\partial x} \left[ b_2 \left( \frac{\partial \Psi}{\partial x} + C \sin \theta \right) \right] = \varepsilon \frac{kg'_s}{\nu} U c_s H(x_{N_b} - x) - w_{d2} C c_s. \tag{2.8}$$

In the above equations, we have introduced the following symbols:

$$U = - \left( \frac{1}{c_s} \frac{\partial b_2}{\partial x} + \frac{\partial h_1}{\partial x} \right) \cos \theta - \sin \theta, \tag{2.9}$$

$$\Psi = \frac{b_2 h_2}{c_s (h_2 - h_1)} \cos \theta, \tag{2.10}$$

$$C = \frac{\bar{c}_2}{c_s} \equiv \frac{b_2}{c_s (h_2 - h_1)}. \tag{2.11}$$

Note that  $U$ ,  $\Psi$  and  $C$  are defined solely for the purpose of simplifying our notation, i.e. these variables do not carry any particular physical meaning. Before studying (2.6)–(2.8) in more detail, it is necessary to define the drainage velocities  $w_{d1}$  and  $w_{d2}$ . These velocities are influenced by the degree of mixing occurring in the lower layer of the porous medium. Because predicting the extent of mixing in this lower layer is a complicated task that relies on numerous factors (see e.g. figure 10 in Bharath *et al.* (2020), and the discussion thereof), we will confine ourselves to two limiting scenarios, which we label as perfect mixing and no mixing. Both of the perfect mixing and no mixing cases are idealizations. Consistent with Pritchard *et al.* (2001), the former assumes that dense fluid that drains through the interbed layer immediately dissolves into lower layer ambient fluid. Meanwhile the latter scenario supposes that mixing details can be ignored in this lower layer (even though they figure prominently in our description of the gravity current flow). Thus we assume that the draining flows evolve as depicted in figure 1. The perfect mixing and no mixing idealizations are helpful bookend-limiting cases that we expect to often bound the true behaviour of the evolving flow.

### 2.1.1. Perfect mixing

As noted above, the perfect mixing regime considers an immediate and total dissolution of drained gravity current fluid when this dense fluid reaches the lower layer. In turn, and because this lower layer is semi-infinite in extent, it maintains a negligible solute concentration. The perfect mixing regime is supposed to be approached when the density difference between the gravity current fluid and the ambient fluid is comparatively large, or when the permeability in the interbed layer is much smaller than elsewhere. As suggested by figure 2, perfect mixing is analogous to a situation where drained fluid is removed from the domain as soon as it exits the interbed layer. Note that such a removal does not

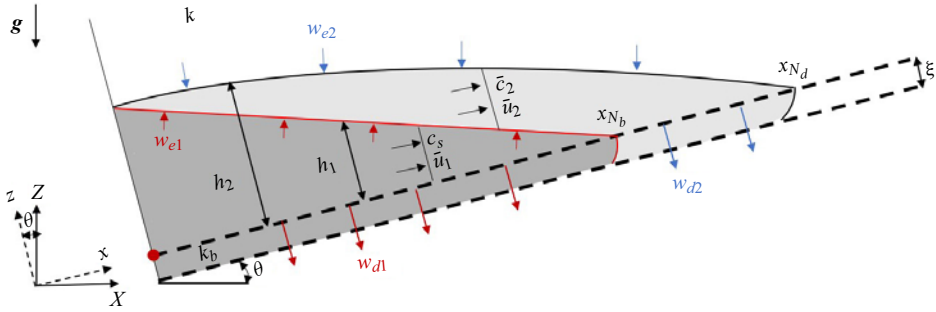


Figure 2. Schematic of a leaky gravity current experiencing perfect mixing in (and therefore immediate removal from) the lower layer. The red line indicates the bulk interface, and the black curve indicates the dispersed interface.

invalidate equations (2.6)–(2.11), which are focused on the flow dynamics in the domain  $z > 0$ .

From figure 2, the drainage velocities  $w_{d1}$  and  $w_{d2}$  can be determined by using the  $z$ -component of Darcy’s law, i.e.

$$\frac{\partial p}{\partial z} = -\rho g' \cos \theta - \frac{\mu}{k} w, \tag{2.12}$$

where  $\mu$  is the dynamic viscosity,  $p$  is the pressure, and  $g' = g\beta c$  is the reduced gravity. We enforce continuity of pressure and of the vertical flux at  $z = 0$ , and thereby conclude that

$$w_{d1}(x, \tilde{t}) = \begin{cases} \frac{k_b g'_s}{\nu} \left( \frac{c_s h_1 + b_2}{c_s \xi} + 1 \right) \cos \theta, & 0 \leq x < x_{N_b}, \\ 0, & x_{N_b} \leq x \leq x_{N_d}. \end{cases} \tag{2.13}$$

This last result considers the draining of bulk phase fluid through the upper and interbed layers. Meanwhile, and by examining the dispersed phase, it can be shown that

$$w_{d2}(x, \tilde{t}) = \begin{cases} 0, & 0 \leq x < x_{N_b}, \\ \frac{k_b g'_s}{\nu} C \left( \frac{h_2}{\xi} + 1 \right) \cos \theta, & x_{N_b} \leq x \leq x_{N_d}. \end{cases} \tag{2.14}$$

(The derivation of (2.13) and (2.14) is outlined in Appendix A.) Note that the (degenerate) limit  $\xi \rightarrow 0$  is not necessarily associated with the appearance of singularities in (2.13) and (2.14) because  $\xi \rightarrow 0$  likewise implies  $k_b \rightarrow 0$ .

### 2.1.2. No mixing

If no mixing occurs in the lower layer, then the solute concentration of the drained fluid is the same as the solute concentration of the gravity current fluid directly above it. In this case, the drainage velocities are obtained by applying (2.12) for both the bulk and dispersed phases and through all three layers of figure 1. That is,

$$w_{d1}(x, \tilde{t}) = \begin{cases} \frac{k_b g'_s}{\nu} \cos \theta \begin{cases} \left( \frac{c_s h_1 + b_2}{c_s l} + 1 \right), & l < \xi, \\ \frac{c_s h_1 + b_2 + c_s l}{(1 - K)c_s \xi + Kc_s l}, & l \geq \xi, \end{cases} & 0 \leq x < x_{N_b}, \\ 0, & x_{N_b} \leq x \leq x_{N_d}, \end{cases} \tag{2.15}$$

and

$$w_{d2}(x, \tilde{t}) = \begin{cases} 0, & 0 \leq x < x_{Nb}, \\ \frac{k_b g'_s}{\nu} \cos \theta \begin{cases} \left(\frac{h_2}{l} + 1\right), & l < \xi, \\ \frac{h_2 + l}{(1 - K)\xi + Kl}, & l \geq \xi, \end{cases} & x_{Nb} \leq x \leq x_{Nd}. \end{cases} \quad (2.16)$$

(The derivation of (2.15) and (2.16) is outlined in Appendix B.) No corresponding expressions are provided for  $u_{d1}$  and  $u_{d2}$  because in the rotated or  $(x, z)$  coordinate system,  $u_{d1}$  and  $u_{d2}$  do not impact the evolution of  $l$ . Here,  $K = k_b/k$  is the permeability ratio. When  $\xi \rightarrow \infty$ , (2.15)–(2.16) are consistent with the drainage formulation of Acton *et al.* (2001) for a gravity current propagating over a deep layer that is permeable but ‘tight’. By contrast, we again avoid consideration of the limit  $\xi \rightarrow 0$ : in the absence of an interbed layer, figure 1 must be redrawn completely because source fluid will now fall vertically in the form of a descending plume. Such a flow, studied at some length by Sahu & Flynn (2015) and Gilmore *et al.* (2021), is not the focus of the current work.

Finally, and in defining the depth of the contaminated fluid in the lower layer, we simplify the analysis by defining  $l(x, \tilde{t})$  as an equivalent depth such that all of the drained fluid in the lower layer has the same uniform solute concentration  $c_s$ . The evolution equation for  $l$  therefore reads

$$\frac{\partial l}{\partial \tilde{t}} = \begin{cases} w_{d1}, & 0 \leq x < x_{Nb}, \\ Cw_{d2}, & x_{Nb} \leq x \leq x_{Nd}. \end{cases} \quad (2.17)$$

In solving (2.17), we acknowledge that we do not distinguish rigorously between the bulk and dispersed phases for  $z < 0$ . On the other hand, no such sacrifice applies for  $z > 0$ , thus our dynamical description of the bulk and dispersed phases of the gravity current is not jeopardized.

### 2.2. Boundary conditions

As shown in Sheikhi *et al.* (2023), boundary conditions for a gravity current consisting of bulk and dispersed phases are

$$-\frac{kg'_s}{\nu} \left[ \left( \frac{1}{c_s} \frac{\partial b_2}{\partial x} + \frac{\partial h_1}{\partial x} \right) h_1 \cos \theta + h_1 \sin \theta \right]_0 = q_s, \quad h_1|_{x_{Nb}} = 0, \quad (2.18a,b)$$

$$h_2|_0 = h_1|_0, \quad h_2|_{x_{Nd}} = 0, \quad (2.18c,d)$$

$$b_2|_0 = 0, \quad b_2|_{x_{Nd}} = 0. \quad (2.18e,f)$$

Whereas the last five of these expressions are self-explanatory, the first (influx) boundary condition merits some additional discussion. In this spirit, (2.18a) signifies that all of the injectate supplied by the source is added to the rear of the gravity current such that the source volume flux matches the gravity current volume flux measured at  $x = 0$ . Thereafter, and consistent with the numerical treatment of the source to be described in § 3, gravity current fluid may propagate down-dip or else drain into the interbed layer.

2.3. Non-dimensional governing equations

Following Goda & Sato (2011), we define a characteristic length scale  $\Pi_1$  and a characteristic time scale  $\Pi_2$  as

$$\Pi_1 = \frac{\nu q_s}{kg'_s} \quad \text{and} \quad \Pi_2 = q_s \left( \frac{\nu}{kg'_s} \right)^2, \tag{2.19a,b}$$

respectively. Thus we define the following dimensionless (starred) variables:

$$\left. \begin{aligned} x^* &= \frac{x}{\Pi_1}, & \xi^* &= \frac{\xi}{\Pi_1}, & h_1^* &= \frac{h_1}{\Pi_1}, & h_2^* &= \frac{h_2}{\Pi_1}, \\ l^* &= \frac{l}{\Pi_1}, & t^* &= \frac{\tilde{t}}{\Pi_2}, & w^* &= w \frac{\Pi_2}{\Pi_1}. \end{aligned} \right\} \tag{2.20a-g}$$

Also,  $c_2^* = c_2/c_s$ . Note that for notational simplicity, we drop the superscript  $*$  such that all variables are now to be interpreted as dimensionless. (By necessity, however, we revert to dimensional variables in § 3.1 and in the appendices.) Accordingly, (2.6)–(2.8) may be rewritten as

$$\frac{\partial h_1}{\partial t} + \frac{\partial(h_1 U)}{\partial x} = -\varepsilon U - w_{d1}, \tag{2.21}$$

$$\frac{\partial h_2}{\partial t} - \frac{\partial}{\partial x} \left[ (h_2 - h_1) \left( \frac{\partial \Psi}{\partial x} + C \sin \theta \right) - h_1 U \right] = -\varepsilon \left( \frac{\partial \Psi}{\partial x} + C \sin \theta \right) - w_{d1} - w_{d2}, \tag{2.22}$$

$$\frac{\partial b_2}{\partial t} - \frac{\partial}{\partial x} \left[ b_2 \left( \frac{\partial \Psi}{\partial x} + C \sin \theta \right) \right] = \varepsilon U H(x_{N_b} - x) - w_{d2} C. \tag{2.23}$$

Here,

$$b_2 = c_2(h_2 - h_1), \tag{2.24}$$

$$U = - \left( \frac{\partial b_2}{\partial x} + \frac{\partial h_1}{\partial x} \right) \cos \theta - \sin \theta, \tag{2.25}$$

$$\Psi = \frac{b_2 h_2}{h_2 - h_1} \cos \theta, \tag{2.26}$$

$$C = \frac{b_2}{h_2 - h_1}. \tag{2.27}$$

Equations (2.21)–(2.23) comprise three equations in three unknowns, namely  $h_1$ ,  $h_2$  and  $b_2$ . The dimensionless boundary conditions to be coupled to these equations read

$$\left[ \left( \frac{\partial b_2}{\partial x} + \frac{\partial h_1}{\partial x} \right) h_1 \cos \theta + h_1 \sin \theta \right]_0 = -1, \quad h_1|_{x_{N_b}} = 0, \tag{2.28a,b}$$

$$h_2|_0 = h_1|_0, \quad h_2|_{x_{N_d}} = 0, \tag{2.28c,d}$$

$$b_2|_0 = 0, \quad b_2|_{x_{N_d}} = 0. \tag{2.28e,f}$$

When a state of perfect mixing can be assumed for the lower layer, the dimensionless drainage velocities that appear in (2.21)–(2.23) are given by

$$w_{d1} = K \cos \theta \begin{cases} \left( \frac{h_1 + b_2}{\xi} + 1 \right), & 0 \leq x < x_{N_b}, \\ 0, & x_{N_b} \leq x \leq x_{N_d}, \end{cases} \tag{2.29}$$

and

$$w_{d2} = K \cos \theta \begin{cases} 0, & 0 \leq x < x_{N_b}, \\ C \left( \frac{h_2}{\xi} + 1 \right), & x_{N_b} \leq x \leq x_{N_d}, \end{cases} \quad (2.30)$$

where  $K$  is the aforementioned permeability ratio. For the no mixing case, by contrast, we write

$$w_{d1} = \begin{cases} K \cos \theta \begin{cases} \left( \frac{h_1 + b_2}{l} + 1 \right), & l < \xi, \\ \frac{h_1 + b_2 + l}{(1 - K)\xi + Kl}, & l \geq \xi, \end{cases} & 0 \leq x < x_{N_b}, \\ 0, & x_{N_b} \leq x \leq x_{N_d}, \end{cases} \quad (2.31)$$

and

$$w_{d2} = \begin{cases} 0, & 0 \leq x < x_{N_b}, \\ K \cos \theta \begin{cases} \left( \frac{h_2}{l} + 1 \right), & l < \xi, \\ \frac{h_2 + l}{(1 - K)\xi + Kl}, & l \geq \xi, \end{cases} & x_{N_b} \leq x \leq x_{N_d}. \end{cases} \quad (2.32)$$

Finally, the non-dimensional analogue of (2.17) becomes

$$\frac{\partial l}{\partial t} = \begin{cases} w_{d1}, & 0 \leq x < x_{N_b}, \\ C w_{d2}, & x_{N_b} \leq x \leq x_{N_d}. \end{cases} \quad (2.33)$$

An explicit finite difference algorithm is employed to solve the governing equations. This approach discretizes spatial derivatives using backward finite differences. Note that, so as to prevent unrealistic singularities, we initialize  $l$  with a small value, i.e.  $l(x, 0) = 10^{-3}$ . Figures 3(a,b) show results for both the perfect mixing and no mixing cases. Because  $l$  is comparable to  $\xi$  at early times, the prediction for  $w_{d1}$  returned by (2.29) is similar to that returned by (2.31), and likewise when considering  $w_{d2}$ , for (2.30) and (2.32). As a result, and up to  $t \simeq 100$ , the gravity current propagates to a comparable extent in both scenarios. As time evolves, the  $l$  predicted by (2.33) for the no mixing case increases steadily. When  $l$  is similar in magnitude to  $h_2$ , the drainage velocity remains small such that the gravity current extends beyond the steady-state value that is realized in the long-time limit. As  $l$  continues to increase, however, the gravity current begins to retract, a pattern clearly evident from figure 3(b). This pattern of extension and retraction is quite different from that noted in the perfect mixing case, where the terminal length of the gravity current is approached monotonically. The difference in behaviour in question therefore provides a convenient metric by which to assess the validity of one versus the other representation of lower layer mixing. However, before elaborating on such details and the results anticipated away from the bookend-limiting cases of figures 3(a,b), it is first necessary to summarize the numerical technique used to resolve such flows.

### 3. Numerical simulations

The first purpose of the COMSOL-based numerical simulations is to approximate the value of  $\varepsilon$  in the theoretical models of § 2. Thereafter, we use numerical results to infer the strengths and weaknesses of the perfect mixing and no mixing models.

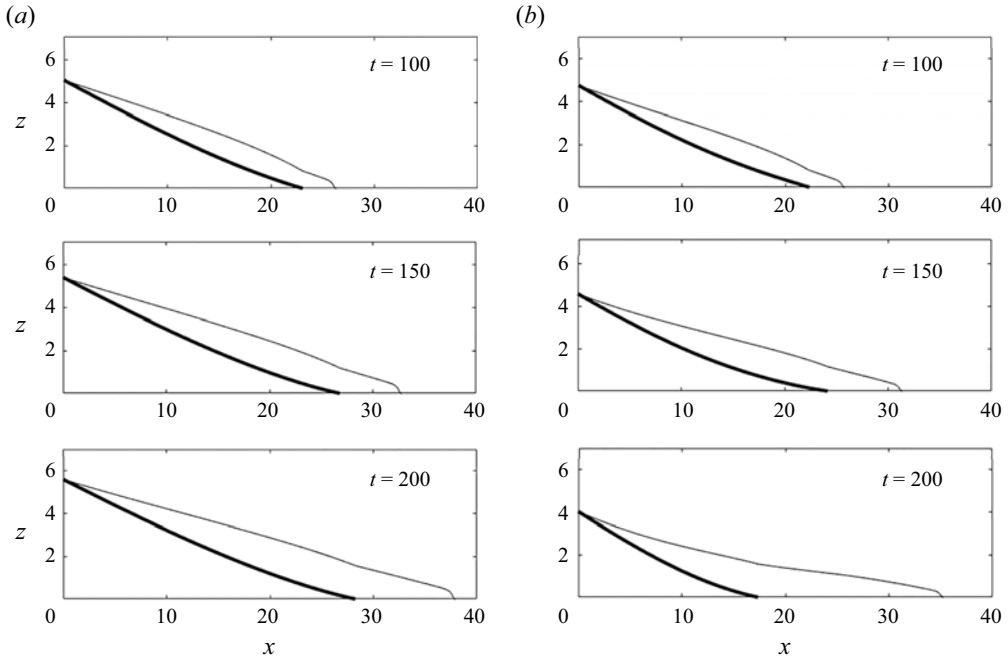


Figure 3. Theoretical predictions showing gravity current profiles assuming (a) perfect mixing, and (b) no mixing in the lower layer. Thick lines represent the bulk interface, and thin lines represent the dispersed interface. Here,  $K = 0.0025$ ,  $\xi = 0.333$  (equivalent to  $K_{eff} \equiv K(1 + 1/\xi) = 0.01$ ) and  $\theta = 0^\circ$ . We further assume that  $\varepsilon = 0.0344$ . The justification for this choice will be presented in § 3.4.

Consistent with the orientation of the flows depicted in figures 1 and 2, we consider the evolution of a dense gravity current through a less dense ambient. More precisely, and mimicking similitude laboratory experiments, we assume that the gravity current and ambient fluids are respectively comprised of salt and fresh water. Although this choice guides our selection of the equation of state, the results of § 4 are, in any event, non-dimensionalized so as to add a degree of generality to our numerically computed calculations. Notwithstanding this preference for non-dimensional variables, it must be noted that  $g'_s = 15$  and  $q_s = 0.3 \text{ cm}^2 \text{ s}^{-1}$  in our simulations. Typically, simulations are run for 20 minutes after injection onset, representing an investment of approximately 30 hours of wall-clock time on an Intel Core i7-9700 CPU with 3.00 GHz and 16 GB memory. (By comparison, solving numerically the theoretical model of § 2 requires only about 3 % of the computational resources needed for the COMSOL simulations.)

### 3.1. COMSOL set-up

In order to determine the velocity and concentration fields in our numerical simulations, mass continuity, Darcy's equation and a solute transport equation are solved. With COMSOL, this is achieved by leveraging the following two interfaces.

- (i) The Darcy's law (dl) interface prescribes the mass and momentum equations as

$$\frac{\partial u}{\partial x} + \frac{\partial w}{\partial z} = 0, \tag{3.1a}$$

*Porous media gravity current flow over an interbed layer*

$$\frac{1}{\rho_0} \frac{\partial p}{\partial x} + \frac{v}{k} u = \frac{\rho}{\rho_0} g \sin \theta, \tag{3.1b}$$

$$\frac{1}{\rho_0} \frac{\partial p}{\partial z} + \frac{v}{k} w = \frac{\rho}{\rho_0} g \cos \theta, \tag{3.1c}$$

respectively.

- (ii) The transport of diluted species in porous media (tds) interface solves the solute transport equation

$$\phi \frac{\partial c}{\partial t} + u \frac{\partial c}{\partial x} + w \frac{\partial c}{\partial z} = \phi \left[ \frac{\partial}{\partial x} \left( D_{xx} \frac{\partial c}{\partial x} + D_{xz} \frac{\partial c}{\partial z} \right) + \frac{\partial}{\partial z} \left( D_{xz} \frac{\partial c}{\partial x} + D_{zz} \frac{\partial c}{\partial z} \right) \right]. \tag{3.2}$$

Here,  $c$  is the solute concentration, and  $D_{xx}$ ,  $D_{xz}$  and  $D_{zz}$  are components of the dispersion tensor,  $D_{ij}$ . As explained by Bear (1972), this tensor can be defined based on two independent variables, namely the longitudinal dispersivity  $a_L$  and the transverse dispersivity  $a_T$ , i.e.

$$D_{xx} = D_{mol} + a_L \frac{u^2}{|V|} + a_T \frac{w^2}{|V|}, \tag{3.3a}$$

$$D_{zz} = D_{mol} + a_L \frac{w^2}{|V|} + a_T \frac{u^2}{|V|}, \tag{3.3b}$$

$$D_{xz} = D_{mol} + (a_L - a_T) \frac{|uw|}{|V|}, \tag{3.3c}$$

where  $D_{mol}$  is the coefficient of molecular diffusion, and  $|V|$  is overall velocity magnitude. Following Sheikhi *et al.* (2023), the dispersivity parameters  $a_L$  and  $a_T$  are predicted based on the empirical correlations of Delgado (2007) as

$$a_L = \begin{cases} 0.5d_p, & 300 < Pe < 10^5, \\ 0.025d_p, & 300 < Pe < 10^5, \end{cases} \quad a_T = 0.025d_p, \tag{3.4a,b}$$

in which  $Pe$  is the Péclet number, and  $d_p$  is the bead diameter. In this work, we consider  $d_p = 0.5$  mm in line with similitude experiments of the type performed by Sahu & Flynn (2017) and Bharath *et al.* (2020). Note finally that the linear equation of state  $\rho = \rho_0 (1 + \beta c)$  allows us to relate the density in (3.1b,c) with the solute concentration in (3.2).

### 3.2. Initial conditions and solver

Initially, it is assumed that the porous medium is filled with fresh water of density  $\rho_0 = 0.998$  g cm<sup>-3</sup> such that the solute concentration is zero at  $t = 0$ . The source consists of an opening, oriented in  $z$ , of height 5 mm across which salt water is injected in  $x$  with a uniform velocity profile. We determine the salt water density from  $g'_s$  by applying

$$\rho_s = \left( 1 + \frac{g'_s}{g} \right) \rho_0. \tag{3.5}$$

To discretize (3.1) and (3.2), an unstructured triangular mesh (with local refinement in the neighbourhood of the source) is employed – see figure 4. After performing a grid independency study, the governing equations are discretized in space using cubic shape functions for (3.1) and quadratic shape functions for (3.2). A third-order implicit backward differentiation formula is employed for time discretization.

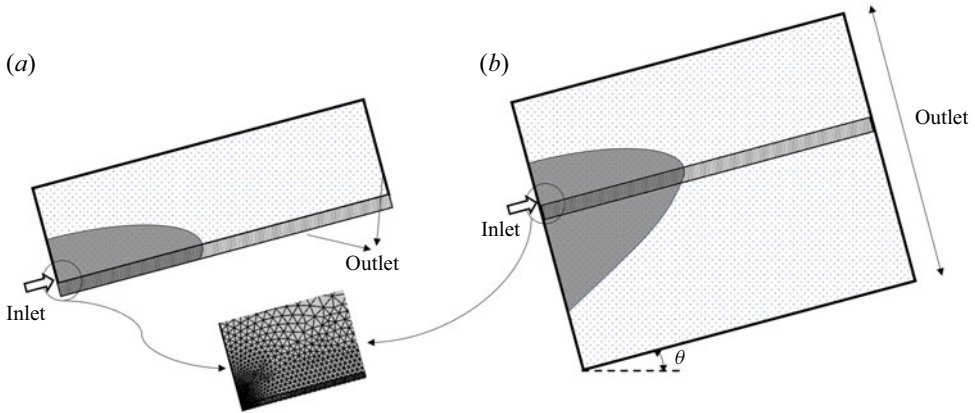


Figure 4. Schematic of the numerical set-up for similitude (a) perfect mixing and (b) laboratory experiments.

### 3.3. Preliminary validation

As described in more detail in Sheikhi *et al.* (2023), our COMSOL model is validated using different points of reference. First, we model the flow of a porous media gravity current along an impermeable boundary and observe strong agreement with the theoretical solution of Huppert & Woods (1995). This comparison confirms the effectiveness of the COMSOL model in predicting porous media buoyancy-driven flow (without either drainage or dispersion). Second, we confirm that our COMSOL model predicts accurately the amount of dispersion experienced by a passive scalar by juxtaposing numerical model output with the classical solution of Bear (1972), § 10.6. This comparison confirms the effectiveness of the COMSOL model in predicting dispersion (without buoyancy effects). Finally, we compare numerical predictions against the flow patterns observed in similitude laboratory experiments of a filling box flow consisting of a leaky gravity current fed by a descending plume, i.e. figures 4(a,c) of Sahu & Flynn (2017). This comparison confirms the effectiveness of the COMSOL model in predicting distributed drainage for flows driven by density differences.

### 3.4. Determination of the entrainment coefficient

Numerical simulations are run under two different mixing scenarios. For one, mixing details in the lower layer are resolved using (3.1) and (3.2), thereby offering the most realistic representation of the flow behaviour expected in, say, a similitude laboratory experiment. For the other, we run numerical experiments that mimic the perfect mixing case of figure 2 and so eliminate dense fluid from the lower layer. This latter category of numerical experiment is run so that, by comparison with the analogue model of § 2, we may estimate the numerical value of the entrainment coefficient  $\varepsilon$ . The value so determined is assumed to apply to both of the perfect mixing and no mixing models, the latter of which is challenging to reproduce numerically. The primary difference between these models concerns, of course, mixing details from the lower layer; in turn, mixing experienced in the domain  $z < -\xi$  seems very unlikely to directly influence mass transport between the bulk and dispersed phases of the gravity current, and therefore the numerical value of the entrainment coefficient.

To make quantitative predictions with our theoretical models, we first have to estimate the value of the entrainment coefficient  $\varepsilon$ . To this end, and with specific reference to the perfect mixing case, the difference between the nose positions of the bulk and dispersed phases in the theoretical versus numerical models is specified by a time-integrated error  $\bar{E}$ , which is defined as

$$\bar{E} = \int_{t_1}^{t_2} \left[ \left( \frac{x_{N_d} - x_{N_b}}{x_{N_d}} \right)_{theory} - \left( \frac{x_{N_d} - x_{N_b}}{x_{N_d}} \right)_{num} \right] dt, \quad (3.6)$$

in which  $((x_{N_d} - x_{N_b})/x_{N_d})_{theory}$  is assessed from the theoretical model, and  $((x_{N_d} - x_{N_b})/x_{N_d})_{num}$  is assessed from the numerical model. When post-processing the numerical data, we follow the approach suggested by Bharath *et al.* (2020) and define  $x_{N_b}$  ( $x_{N_d}$ ) as the down-dip-most location where fluid having density 80% (5%) of the source density can be found. Note also that we select  $t_1 = 20$  (by which time the gravity current is indeed long and thin) and  $t_2 = 200$  (by which time the gravity current has propagated a significant distance downstream). The  $\varepsilon$  that minimizes this time-integrated error is considered as the optimum value for the entrainment coefficient in the theoretical model.

For mathematical simplicity, the theoretical models of § 2 assume a linear relationship between  $w_{ei}$  and  $u_i$ , where  $i = 1, 2$ . However, and consistent with the free shear flow study of van Reeuwijk, Holzner & Caulfield (2019) and the porous media flow study of Sheikhi *et al.* (2023), we allow the entrainment coefficient to vary with the dip angle  $\theta$ , and also with  $K_{eff}$ , defined as

$$K_{eff} = K \left( 1 + \frac{1}{\xi} \right). \quad (3.7)$$

Here,  $K_{eff}$  is motivated by the functional forms of (2.29) and (2.30), which demonstrate that the draining velocities depend directly on  $K$  and  $\xi^{-1}$ . In physical terms,  $K_{eff}$  characterizes the ease with which dense fluid may drain through the interbed layer. Resistance to draining may arise because  $K$  is relatively small or because  $\xi$  is relatively large (though not so large that the interbed thickness is large compared to a characteristic gravity current thickness);  $K_{eff}$  takes into account both of these considerations. The resistance to draining may arise because of either the value of  $K$  or the value of  $\xi$ ;  $K_{eff}$  takes into account both of these considerations. Thus larger  $K_{eff}$  is associated with more draining and with a slower speed of advance for the gravity current. Corresponding data are summarized in figure 5. These results suggest that  $\varepsilon$  increases with both of  $\theta$  and  $K_{eff}$ . In this way, our results, though consistent with the porous media flow investigation of Sheikhi *et al.* (2023), demonstrate an intriguing difference with van Reeuwijk *et al.* (2019). Although they likewise determined that  $\varepsilon$  increases with  $\theta$ , their investigation pertained to downslope, not upslope, flow. In other words, van Reeuwijk *et al.* (2019) determined that the entrainment coefficient increases with the gravity current speed, whereas porous media flows evidently exhibit the opposite behaviour. This difference is likely related to the different entrainment mechanisms that apply for turbulent free shear flows versus porous media flows. In the former case, entrainment is a consequence of large-scale eddies, which entrain external ambient fluid via engulfment. Even for small  $\theta$ , no such mechanism applies for the porous media flows of interest here, which remain laminar such that gravity current boundaries remain smooth. Graphical evidence for this last claim is presented in the next section.

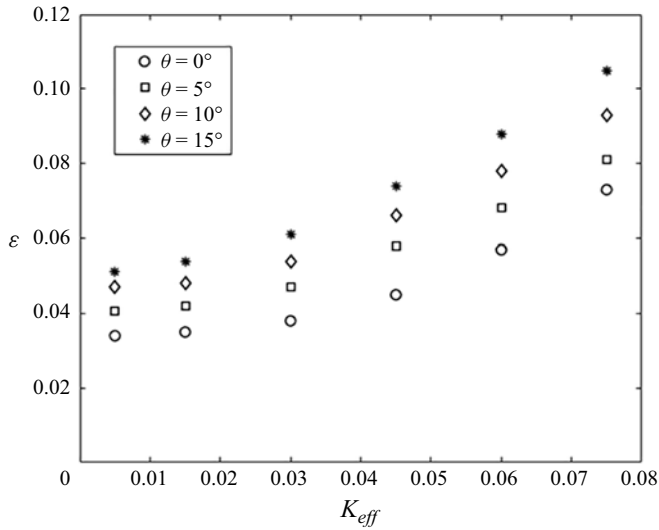


Figure 5. Error-minimizing value of  $\varepsilon$  versus  $\theta$  and  $K_{eff} = K(1 + 1/\xi)$ .

## 4. Results and discussion

### 4.1. Comparison of theoretical and numerical results

Figure 6 compares the numerical output against the theoretical predictions made by the perfect mixing and no mixing models. As anticipated, the numerical solution often lies between the two extremes of perfect (red curves) versus no mixing (black curves). Consistent with figure 3, the black and red curves very nearly overlap at early times, but then diverge as  $t$  increases. By extension, and for both  $\theta = 0^\circ$  and  $\theta = 5^\circ$ , there is good qualitative agreement between the numerical data and the theoretical predictions for  $t \lesssim 100$ . For  $t \gtrsim 100$ , the perfect mixing model continues to provide reasonably accurate predictions for the shape and extent of the bulk and dispersed phases. On the other hand, the accuracy of the no mixing model suffers from its over-prediction of gravity current retraction. Additional discussion on this point is provided below.

Shown in figures 7(a–b) are the bulk nose positions, and in figures 7(c–d) the dispersed nose positions, for the two theoretical models. Also included in figure 7 are corresponding numerical data, which are indicated by the solid symbols. The no mixing model predicts a gradual retraction in the bulk phase but an abrupt retraction in the dispersed phase. As the inset images in figure 7 make clear, the sudden retraction in the dispersed phase occurs because of a decrease in the thickness of the dispersed phase at its leading edge. The decrease in question causes a sudden vanishing of the thinned front. As the effective permeability  $K_{eff}$  increases, the drainage becomes more robust, and the equivalent drained depth  $l$  increases more quickly. The retraction, therefore, occurs earlier for larger  $K_{eff}$ . Beyond the onset of retraction, draining is so robust, and vertical velocities in the gravity current so large, that the assumption of a hydrostatic flow can no longer be justified. In figure 7, the (black) line type then changes from solid to dashed. Figure 7 confirms that the degree of gravity current retraction experienced in the numerical model, though non-zero, is small and time-delayed, much more so than is predicted by the no mixing model. So although the no mixing model gives predictions that are in reasonably good agreement with the numerical data up to the point of retraction, model fidelity suffers thereafter. Generally more favourable agreement is observed when considering the perfect mixing

*Porous media gravity current flow over an interbed layer*

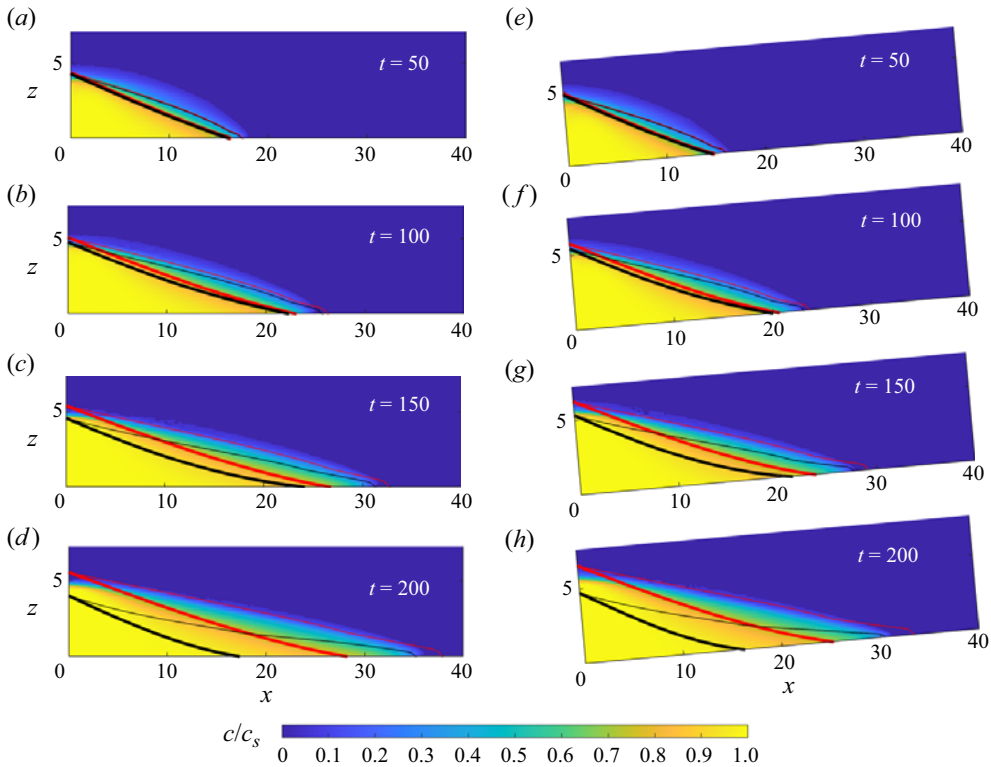


Figure 6. Numerical prediction of the gravity current profile versus the analogue theoretical predictions corresponding to perfect mixing (red curves) and no mixing (black curves). Thick lines indicate the bulk interface, and thin lines indicate the dispersed interface. The colour contours show the numerical output: (a–d)  $\theta = 0^\circ$ , and (e–h)  $\theta = 5^\circ$ . Here,  $K = 0.0025$  and  $\xi = 0.333$ , which is equivalent to  $K_{eff} = 0.01$ .

model, although the long-time limit is characterized by an over-prediction of the front positions for both the bulk and dispersed phases. Not surprisingly, deviations are seen to increase as draining is made more robust, i.e. as the value of  $K_{eff}$  increases.

The results of figure 7, in particular the observation concerning the eventual non-hydrostatic nature of the flow in the no mixing case, motivate us to divide the  $(t, K_{eff})$  parameter space as in figure 8. The red region shows the regime before the onset of gravity current retraction in the no mixing model. In this red regime, we can use either theoretical model to predict, with reasonable accuracy, the forward advance of the bulk and dispersed phases. The green area shows the regime where the no mixing model becomes unduly influenced by its prediction of gravity current retraction. Here, the no mixing model generates results that are consistent with respect to the model assumptions but not, unfortunately, in good agreement with numerically determined behaviour. The severity of the retraction predicted by the no mixing model stems from its inability to account for the instabilities that develop within the lower layer draining fluid. We elaborate on this point in § 4.3. Thereafter, and in the blue region of figure 8, the flow predicted by the no mixing model becomes non-hydrostatic, and the model violates one of the key assumptions stated in § 2. In this blue region, therefore, only the perfect mixing model is physically acceptable. Finally, when  $K_{eff}$  exceeds approximately 0.075, corresponding to the white region in figure 8, the drainage velocity becomes so large that the hydrostatic assumption is violated

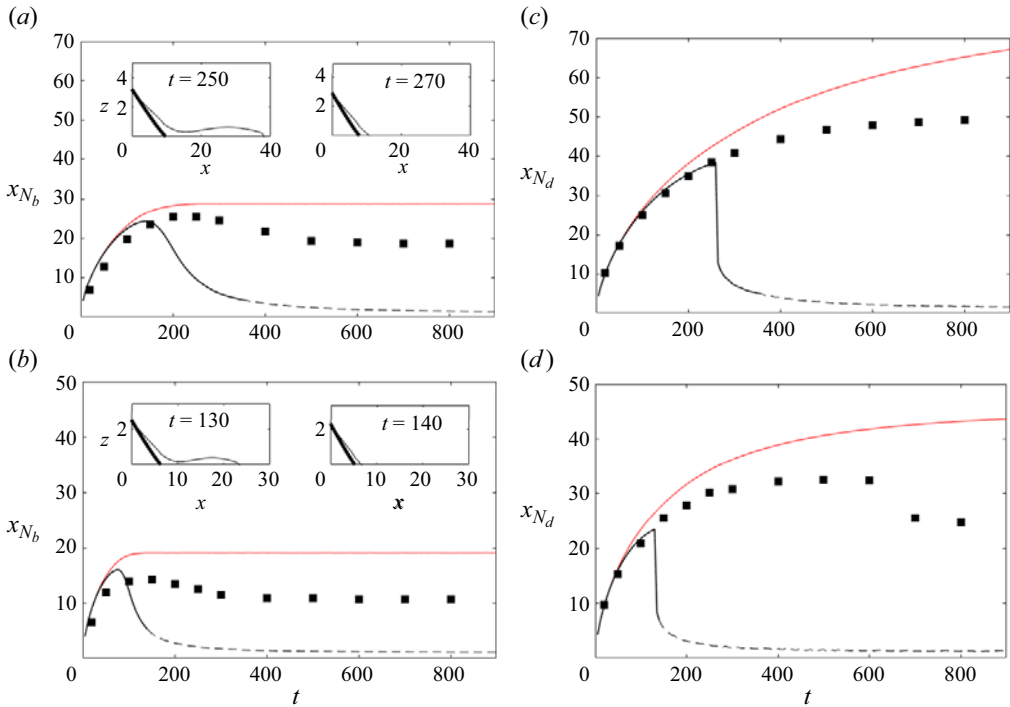


Figure 7. Time series of the bulk and dispersed nose positions for  $\theta = 0^\circ$  and (a,c)  $K_{eff} = 0.01$  and (b,d)  $K_{eff} = 0.02$ . Numerical data are indicated by the square symbols; theoretical predictions are indicated by the red (perfect mixing) and black (no mixing) curves. The dashed black curves indicate the domain where the hydrostatic assumption becomes invalid in the no mixing model. The inset images show the bulk and dispersed interfaces before and after the sharp reduction in the position  $x_{N_d}$  of the dispersed nose for the no mixing case.

even in the perfect mixing model. In this regime, most of the injectate immediately drains to the lower layer such that relatively little fluid remains above the permeability jump in the form of a distinct gravity current. Separate analyses (not shown) suggest that the regime diagram of figure 8 is insensitive to the choice of inclination angle. Accordingly, the results of figure 8 are presumed applicable for different  $\theta$ .

#### 4.2. Effects of $K_{eff}$ and $\theta$ on dispersion

In this subsection, attention is restricted to the case where both theoretical models yield accurate predictions corresponding to the red region of figure 8. In this red region, we can employ the no mixing and perfect mixing models to quantify the impact on dispersion of two especially important dimensionless parameters, namely  $K_{eff}$  and  $\theta$ . To this end, we consider as dispersion metrics the separation distance between the bulk and the dispersed nose positions, and the fraction of the total buoyancy (per unit width) that is specifically associated with the dispersed phase. As regards the latter parameter, and with respect to the thick and thin curves of figure 3, we first calculate

$$B_{bulk} = \int_0^{x_{N_b}} h_1 dx \quad \text{and} \quad B_{disp} = \int_0^{x_{N_d}} c_2(h_2 - h_1) dx \equiv \int_0^{x_{N_d}} b_2 dx. \quad (4.1a,b)$$

Porous media gravity current flow over an interbed layer

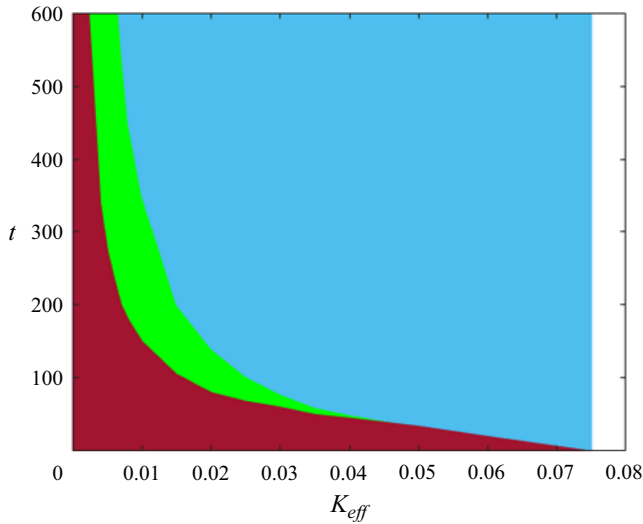


Figure 8. Theoretical model regime diagram illustrating the regimes where (i) both of the no mixing and perfect mixing models return accurate predictions (red), (ii) the no mixing model remains hydrostatic but is inaccurate owing to its over-prediction of gravity current retraction (green), (iii) the no mixing model is invalid (blue) and (iv) both models become invalid (white). Formally, data are shown for  $\theta = 0^\circ$ ; however, we find very similar results at different inclination angles.

The dispersed buoyancy fraction  $\tilde{B}_{disp}$  is then found from

$$\tilde{B}_{disp} = \frac{B_{disp}}{B_{bulk} + B_{disp}}. \quad (4.2)$$

The sensitivity of dispersion to  $K_{eff}$  is explored in figure 9. Figure 9(a) shows the nose separation  $1 - x_{N_b}/x_{N_d}$ , whereas figure 9(b) shows the dispersed buoyancy fraction  $\tilde{B}_{disp}$ . In both plots, data are measured at  $t = 150$ . Increasing  $K_{eff}$  leads to more drainage of bulk fluid from the gravity current, which thereby retards the elongation of the bulk phase. Although increasing  $K_{eff}$  likewise increases the drainage of dispersed fluid, the effect is comparatively mild, so the net effect of increasing the effective permeability is to increase both the nose position separation distance and also the dispersed buoyancy fraction. The trends in question are apparent from both of the no mixing (black curves) and perfect mixing (red curves) models, and are also evident from the superposed numerical data (closed symbols). Consistent with figure 7, and for the relatively modest values of  $t$  of interest here, we find better agreement between the numerical data and the predictions of the no mixing model versus the perfect mixing model.

A complementary comparison but considering the impact of  $\theta$  rather than  $K_{eff}$  is presented in figure 10. When the bottom boundary is inclined up-dip such that  $\theta > 0^\circ$ , the gravity current characteristic velocity decreases. Hence entrainment to the dispersed phase, whether from the surroundings or from the bulk phase, is reduced. Therefore, both of  $1 - x_{N_b}/x_{N_d}$  and  $\tilde{B}_{disp}$  decrease with  $\theta$ . Comparing figure 10 against figure 9 shows that dispersion intensity is more sensitive to  $K_{eff}$  than to  $\theta$ , e.g. doubling the former parameter yields a bigger change in  $1 - x_{N_b}/x_{N_d}$  and  $\tilde{B}_{disp}$  than is realized by doubling the latter parameter. On the other hand, and as with figure 9, figure 10 confirms that output from the numerical simulations is better aligned with the no mixing model than with its perfect mixing counterpart.

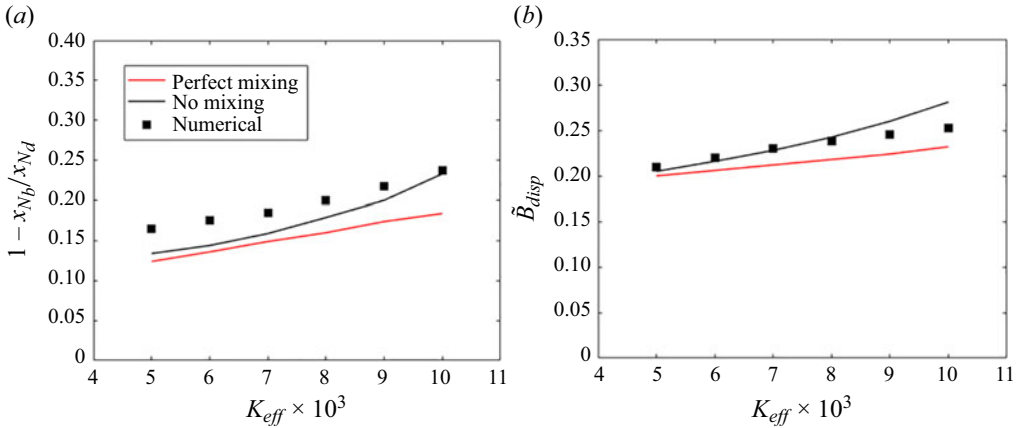


Figure 9. (a) Difference of nose separation and (b) buoyancy fraction in the dispersed phase for  $\theta = 0^\circ$  but various  $K_{eff}$  at  $t = 150$ .

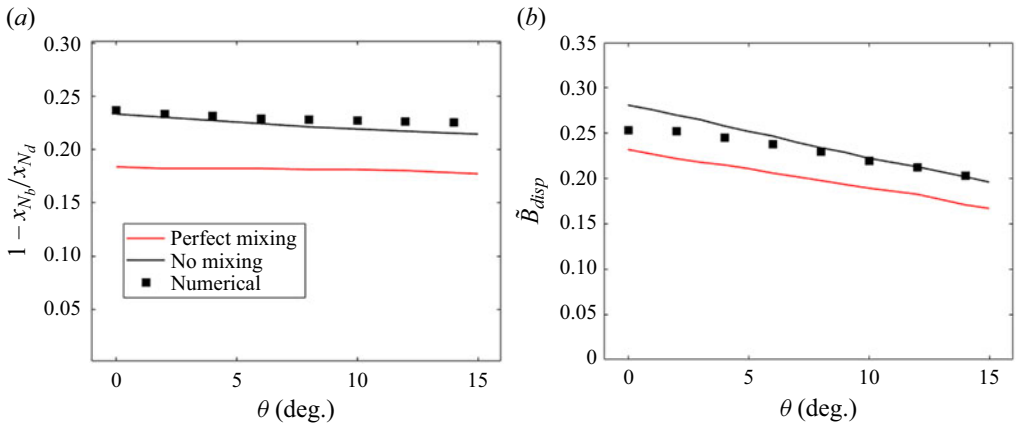


Figure 10. As in figure 9 but considering the influence of  $\theta$  for  $K_{eff} = 0.01$ .

#### 4.3. Flow characterization past the point of theoretical model breakdown

Although the theoretical models of § 2 become inaccurate and/or invalid in the green and blue regions of figure 8, we can leverage the numerical results from the COMSOL simulations to investigate the flow behaviour within these parameter spaces. These numerical simulations illustrate that following the elongation of both the bulk and dispersed phases, the bulk phase begins to retract, whereafter the dispersed phase begins to thin – see figures 11(a,b). The thin leading edge of the dispersed phase eventually disappears, and the bulk and dispersed phases reach their respective terminal lengths. Qualitatively similar behaviour is predicted by the no mixing model – see e.g. figure 7 – though in this theoretical case, transitions are more abrupt and the magnitude of the retraction is much larger.

Examination of the numerical data has a further benefit, namely that it allows us to study the details of the draining flow. To this end, figure 12 shows the convective flow patterns that develop in the lower layer for different  $K_{eff}$ . Figure 12 confirms that drainage is more severe for  $0 \leq x < x_{Nb}$ , than it is for  $x_{Nb} \leq x \leq x_{Nd}$ . Moreover, and consistent with

*Porous media gravity current flow over an interbed layer*

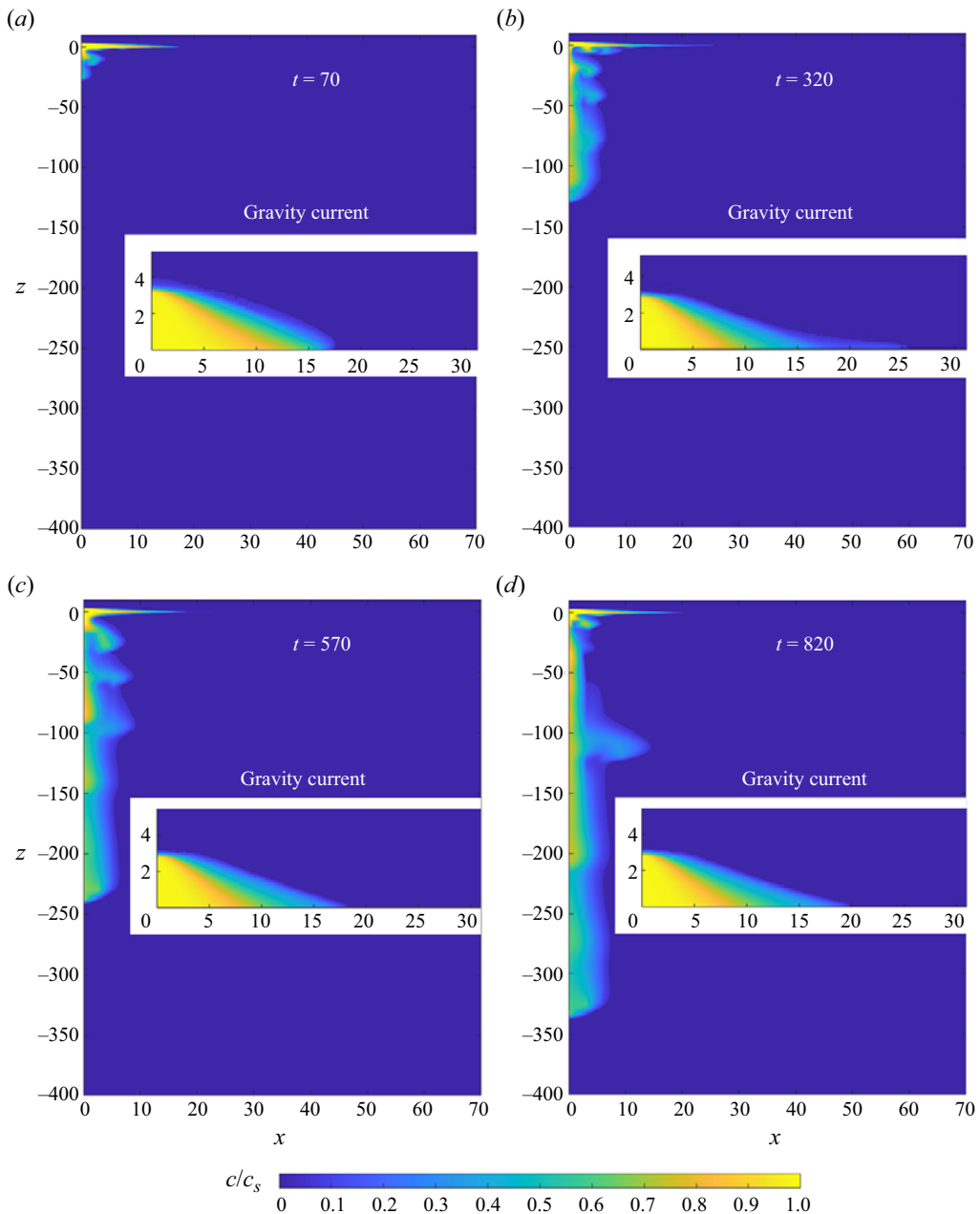


Figure 11. Numerical prediction of the flow in the green and blue regions of figure 8. Inset images show the gravity current profile in more detail. Here,  $K_{eff} = 0.03$ ,  $\theta = 0^\circ$ , and non-dimensional times are as indicated.

Leahy *et al.* (2009) and Sahu & Neufeld (2023), this figure demonstrates the presence of fingers, which result from a Rayleigh–Taylor-type instability. The appearance of fingers is characterized by alternating bands of upward- versus downward-propagating fluid – see e.g. the solid red curve in figure 12(a). Moreover, the bulbous shape of the largest finger from figure 12(b) suggests an eventual separation of this draining fluid from the overlying gravity current. In either case, the situation differs significantly from the much more

https://doi.org/10.1017/jfm.2024.203 Published online by Cambridge University Press

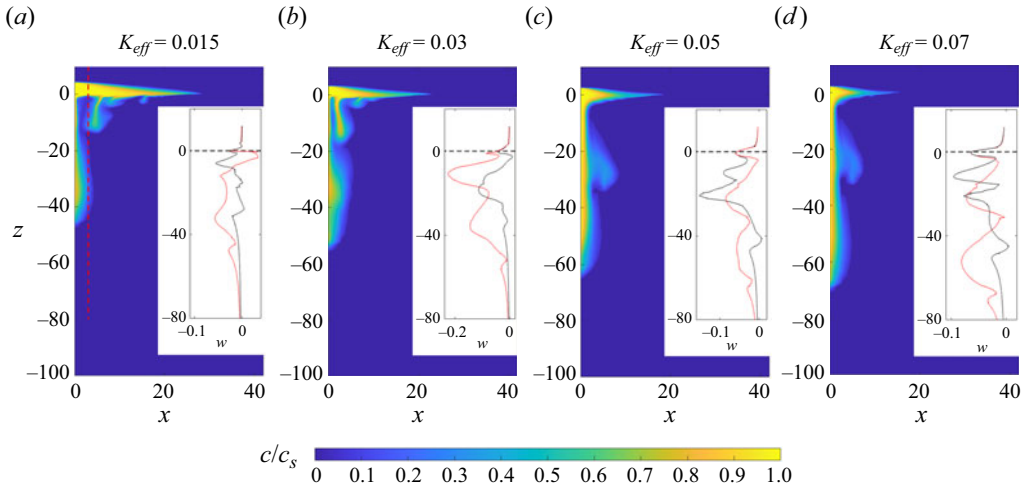


Figure 12. Numerical prediction of the gravity current and associated draining flow for different  $K_{eff}$  at  $t = 150$ , with  $\theta = 0^\circ$ . The inset images show the vertical variation of the vertical velocity,  $w$ . Curves are drawn for  $t = 100$  (black lines) and  $t = 150$  (red lines). The red dashed line in (a) displays the location  $x = 3$ , where vertical velocities are evaluated.

$\theta = 0^\circ$		$\theta = 5^\circ$	
$K_{eff}$	$\tilde{B}_{disp}$	$K_{eff}$	$\tilde{B}_{disp}$
0.015	0.80	0.015	0.83
0.03	0.85	0.03	0.68
0.05	0.65	0.05	0.59
0.07	0.77	0.07	0.60

Table 1. Lower layer dispersed buoyancy fraction at  $t = 150$  for various  $K_{eff}$  and  $\theta = 0^\circ, 5^\circ$ .

uniform scenario associated with the no mixing model, whereby the vertical velocities measured in the gravity current, the interbed layer and the lower layer are identical (and over-predicted). Note finally that as  $K_{eff}$  increases, fingers form earlier. With reference to [figure 8](#), this explains why the time interval over which the theoretical models work well is tighter for larger  $K_{eff}$ .

To categorize mixing in the lower layer, we can extend the definition of  $\tilde{B}_{disp}$  to the draining flow. Accordingly, we evaluate integrals similar to those of (4.1a,b) but spanning a vertical domain  $z < -\xi$ . Thus we suppose that  $\tilde{B}_{disp}$  now represents the fraction of the drained fluid that appears in a dispersed rather than in a bulk phase. Numerical values for the redefined  $\tilde{B}_{disp}$  are reported in [table 1](#) for various  $K_{eff}$  and for two inclination angles, i.e.  $\theta = 0^\circ$  and  $\theta = 5^\circ$ .

Although there is some scatter in the data, particularly for the case of a horizontal permeability jump, the results of [table 1](#) support the conclusion that most of the drained fluid exists in a dispersed state, especially for small  $K_{eff}$ . This observation is helpful in the re-examination of [figure 7\(a\)](#), particularly over the time interval  $200 \lesssim t \lesssim 350$ . There, we find much better overall agreement between the numerical data and the perfect mixing model (red curve) than the no mixing model (black curve). The no mixing model fails to account for the dispersed (and disconnected) nature of the drained flow

and so over-predicts both the influence of dense fluid from the lower layer and the severity of gravity current retraction. This limitation is obviously avoided by the perfect mixing model, which neglects any contribution of the drained flow when calculating the draining velocity. The perfect mixing model thereby provides a more accurate (though still imperfect) prediction for the distances travelled by each of the bulk and dispersed phases.

## 5. Summary and conclusions

The present analysis considers, theoretically and numerically, the flow of a porous media gravity current along an interbed layer where drainage from the gravity current underside is spatially distributed. The theoretical model of § 2 includes dispersive mixing and separates the gravity current into bulk and dispersed phases. The latter phase entrains fluid from the former and also from the surrounding ambient. For expediency, we adopt a somewhat simpler approach when considering the evolution of the fluid that drains into the lower layer of the porous medium. Thus we restrict attention to the two bookend opposite cases of no mixing versus perfect mixing. The non-dimensional governing equations presented in § 2 make reference to two dimensionless parameters, namely  $K_{eff}$ , the effective permeability defined by (3.7), and  $\theta$ , the inclination angle of the interbed layer. Increasing  $K_{eff}$  by either increasing the permeability of the interbed layer or else decreasing its thickness intensifies drainage from both the bulk and dispersed phases. Given that drainage is notably more severe in the bulk phase, increasing  $K_{eff}$  (i) yields a larger separation between the bulk and dispersed nose positions, and (ii) causes a greater fraction of the gravity current fluid to reside in the dispersed phase. By either metric, we conclude that dispersion is more significant. Increasing  $\theta$ , so that the gravity current flows up a steeper incline, leads to a smaller velocity of advance and therefore to less dispersion. Our analysis (see e.g. figure 8) suggests that, consistent with Sahu & Neufeld (2023), the hydrostatic pressure assumption becomes invalid when  $K_{eff}$  and  $t$  are large. The no mixing and perfect mixing models do not, therefore, provide meaningful predictions always. In particular, the no mixing model eventually predicts a draining velocity that is too large and so exhibits a more limited range of applicability than its perfect mixing counterpart.

To gain additional insights into the veracity of our model predictions, we ran a series of complementary COMSOL numerical simulations as described in § 3. In the first case, numerical data are needed to calibrate the value of the entrainment coefficient  $\varepsilon$  that appears in the governing equations (2.21)–(2.23). Figure 5 demonstrates that the optimum value of  $\varepsilon$  is a function of  $K_{eff}$  and  $\theta$ . (Note that we consider the same value for  $\varepsilon$  for both of the no mixing and perfect mixing models because the entrainment coefficient depends on the details of the dispersive mixing that occurs between the gravity current and the ambient, but not on mixing processes in the lower layer.) In the second case, numerical simulations are performed for the sake of comparison with theoretical model output. Not surprisingly, the numerical simulations require approximately 30 times the number of floating point operations given e.g. the simplifying assumptions applied in the theoretical model. Figures such as 6, 7, 9 and 10 confirm that both theoretical models provide a reasonable description of the gravity current evolution, at least until the point where the no mixing model predicts flow retraction. Thereafter, the front positions anticipated by the no (perfect) mixing model significantly under-predict (moderately over-predict) the numerically derived behaviour. The eventual breakdown of the no mixing model cannot be regarded as surprising: the model assumes that fluid drained to the lower layer contributes to basal draining in perpetuity. This picture is rather different from the numerical simulation results of figure 12, which suggest the appearance of convective

fingers that both mix into the lower layer ambient and later detach from gravity current underside. Fingers are the result of a Rayleigh–Taylor-type instability, are characterized by adjacent bands of upward- versus downward-directed flow, and materialize earlier for larger  $K_{eff}$ . On the other hand, and for smaller  $K_{eff}$ , we observe that a greater fraction of the draining fluid in the lower layer appears in a dispersed rather than bulk phase – see e.g. [table 1](#). This is, of course, the opposite behaviour to what is observed in the upper layer. In other words, large  $K_{eff}$  is associated with robust dispersion above the interbed layer, but comparatively modest dispersion below. Meanwhile, small  $K_{eff}$  is associated with more modest dispersion above the interbed layer, but more robust dispersion below. These observations suggest that theoretical models that consider sharp interfaces for the gravity current and also for the draining fluid may apply only under special circumstances, e.g. at relatively early times before finger onset.

Although we have presented a careful comparison of theory and numerical simulation, it remains to confirm independently the accuracy of both categories of models with similitude laboratory experiments. To this end, we envision running a series of experiments in the spirit of Huppert, Neufeld & Strandkvist (2013), Bharath *et al.* (2020) and Sahu & Neufeld (2023). In such a case, the interbed layer may be included by application of a thin porous substrate as in the experiments of Thomas, Marino & Linden (1998). Laboratory experiments must employ a lower layer of large depth so as to avoid the collision of the draining fluid with the bottom boundary of the tank. If such a collision were to occur, then a secondary gravity current would appear, which has the potential to influence the evolution of the gravity current propagating along the interbed layer – see e.g. Bharath & Flynn (2021). Turning from the laboratory to the field, it is important to reiterate that our research is motivated by examples of environmental flows in geological layers. These are more complicated than the physical domain that we consider here, owing, for instance, to the more complicated pattern of layer heterogeneities than is accounted for in [figure 1](#). In the next step, it would be beneficial to include multiple interbed layers, as has been done in the studies of Neufeld & Huppert (2009), Behnam, Bickle & Neufeld (2021) and Sahu & Neufeld (2023), for example. By doing so, we can better understand buoyancy-driven flow through non-uniform porous media, e.g. the communication of  $H_2$  between different layers in underground hydrogen storage (UHS) projects involving depleted natural gas reservoirs. Our models also consider that the dynamic viscosity  $\mu$  is independent of the concentration and is therefore the same in the bulk and dispersed phases. For the UHS example described in the Introduction, the viscosity of the dispersed phase (consisting of a mixture of  $H_2$  and  $CH_4$ ) should be more than that of the bulk phase (consisting of  $H_2$ ). Underestimating the dispersed phase viscosity leads to over-predicting its propagation speed. Relative to real geological flows, the models presented here might therefore over-predict the extent of dispersion. Quantifying this effect more precisely is a topic of current interest; to this end, we hope to report on our findings in a future publication.

**Funding.** This research is supported by NSERC (Discovery Grant programme).

**Declaration of interests.** The authors report no conflict of interest.

**Author ORCIDs.**

 S. Sheikhi <https://orcid.org/0000-0002-8306-8806>;

 M.R. Flynn <https://orcid.org/0000-0002-7559-9463>.

**Appendix A. Derivation of the drainage velocity in the perfect mixing model**

With reference to [figure 2](#), we assume a hydrostatic pressure distribution through the gravity current such that the pressures measured along  $z = 0$  in the bulk and dispersed phases are

$$p_{1,I}(x, 0, \tilde{t}) = \rho_0 g'_s \left( h_1 + \frac{b_2}{c_s} \right) \cos \theta + P_0 + \rho_0 g x \sin \theta, \tag{A1}$$

$$p_{2,I}(x, 0, \tilde{t}) = \rho_0 g'_s C h_2 \cos \theta + P_0 + \rho_0 g x \sin \theta, \tag{A2}$$

respectively. Here, subscript  $I$  indicates the upper layer of [figure 2](#). Turning to the interbed layer, we integrate Darcy's law in the  $z$ -direction below the bulk and dispersed phases and find that

$$\int_z^0 \frac{\partial p_{1,II}}{\partial z} dz = - \int_z^0 \rho_0 g'_s \cos \theta dz - \int_z^0 \frac{\mu}{k_b} w_{d1} dz, \tag{A3}$$

$$\int_z^0 \frac{\partial p_{2,II}}{\partial z} dz = - \int_z^0 \rho_0 C g'_s \cos \theta dz - \int_z^0 \frac{\mu}{k_b} w_{d2} dz, \tag{A4}$$

in which subscript  $II$  denotes the interbed layer. Fortunately, all terms under the right-hand-side integrals of (A3) and (A4) are independent of  $z$ , and the integrals are therefore straightforward to evaluate. Consistent with Acton *et al.* (2001) and by considering pressure continuity at  $z = 0$  such that  $p_{1,I}(x, 0, \tilde{t}) = p_{1,II}(x, 0, \tilde{t})$  and  $p_{2,I}(x, 0, \tilde{t}) = p_{2,II}(x, 0, \tilde{t})$ , the pressure distributions through the interbed layer are given by

$$p_{1,II}(x, z, \tilde{t}) = \rho_0 g'_s \left( h_1 + \frac{b_2}{c_s} - z \right) \cos \theta - \frac{\mu}{k_b} w_{d1} z + P_0 + \rho_0 g x \sin \theta, \tag{A5}$$

$$p_{2,II}(x, z, \tilde{t}) = \rho_0 g'_s C (h_2 - z) \cos \theta - \frac{\mu}{k_b} w_{d2} z + P_0 + \rho_0 g x \sin \theta, \tag{A6}$$

for the bulk and dispersed phases, respectively. Also following Acton *et al.* (2001), we set  $p_{1,II}(x, -\xi, \tilde{t}) = P_0 + \rho_0 g x \sin \theta$  and  $p_{2,II}(x, -\xi, \tilde{t}) = P_0 + \rho_0 g x \sin \theta$ . Using these results, the drainage velocities for the perfect mixing case can be recovered by substituting  $z = -\xi$  in (A5) and (A6), then solving for  $w_{d1}$  and  $w_{d2}$ , respectively. So we find that

$$w_{d1}(x, \tilde{t}) = \begin{cases} \frac{k_b g'_s}{\nu} \left( \frac{c_s h_1 + b_2}{c_s \xi} + 1 \right) \cos \theta, & 0 \leq x < x_{N_b}, \\ 0, & x_{N_b} \leq x \leq x_{N_d}, \end{cases} \tag{A7}$$

and

$$w_{d2}(x, \tilde{t}) = \begin{cases} 0, & 0 \leq x < x_{N_b}, \\ \frac{k_b g'_s}{\nu} C \left( \frac{h_2}{\xi} + 1 \right) \cos \theta, & x_{N_b} \leq x \leq x_{N_d}. \end{cases} \tag{A8}$$

**Appendix B. Derivation of the drainage velocity in the no mixing model**

Using (A5) and (A6), the pressures measured at the base  $z = -\xi$  of the interbed layer of figure 1 are

$$p_{1,II}(x, -\xi, \tilde{t}) = \rho_0 g'_s \left( h_1 + \frac{b_2}{c_s} + \xi \right) \cos \theta + \frac{\mu}{k_b} w_{d1} \xi + P_0 + \rho_0 g x \sin \theta, \tag{B1}$$

$$p_{2,II}(x, -\xi, \tilde{t}) = \rho_0 g'_s C(h_2 + \xi) \cos \theta + \frac{\mu}{k_b} w_{d2} \xi + P_0 + \rho_0 g x \sin \theta. \tag{B2}$$

If we consider, consistent with Neufeld & Huppert (2009), the continuity of flux perpendicular to the boundary at  $z = -\xi$ , then the drainage velocities  $w_{d1}$  and  $w_{d2}$  must be constant through the interbed and lower layers. Regarding this lower layer, we integrate Darcy’s law in the  $z$ -direction and find that

$$\int_z^{-\xi} \frac{\partial p_{1,III}}{\partial z} dz = - \int_z^{-\xi} \rho_0 g'_s \cos \theta dz - \int_z^{-\xi} \frac{\mu}{k} w_{d1} dz, \tag{B3}$$

$$\int_z^{-\xi} \frac{\partial p_{2,III}}{\partial z} dz = - \int_z^{-\xi} \rho_0 C g'_s \cos \theta dz - \int_z^{-\xi} \frac{\mu}{k} w_{d2} dz. \tag{B4}$$

Again, all of the terms under the right-hand-side integrals are independent of  $z$ . Note that for the sake of mathematical convenience, we suppose that any drained fluid that appears in the lower layer forms a uniform layer of depth  $l$ . This simplification is in obvious contrast to figure 1, which defines layer depths  $l_1$  and  $l_2$  for the bulk and dispersed phases, respectively. As a consequence of the simplification, it is appropriate to set  $C = 1$  in the former right-hand-side terms of (B2) and (B4). By assuming pressure continuity at  $z = -\xi$ , the pressure distributions under the gravity current bulk phase and dispersed phase can be found. These read

$$p_{1,III}(x, z, \tilde{t}) = \rho_0 g'_s \left( h_1 + \frac{b_2}{c_s} - z \right) \cos \theta + \frac{\mu}{k_b} w_{d1} [(1 - K)\xi - Kz] + P_0 + \rho_0 g x \sin \theta, \tag{B5}$$

$$p_{2,III}(x, z, \tilde{t}) = \rho_0 g'_s (h_2 - z) \cos \theta + \frac{\mu}{k_b} w_{d2} [(1 - K)\xi - Kz] + P_0 + \rho_0 g x \sin \theta. \tag{B6}$$

Consistent with Acton *et al.* (2001), we set  $p_{1,III}(x, -l, \tilde{t}) = p_{2,III}(x, -l, \tilde{t}) = P_0 + \rho_0 g x \sin \theta$ . Combining this information with (B5) and (B6), the drainage velocities in the no mixing case can be written as

$$w_{d1}(x, \tilde{t}) = \begin{cases} \frac{k_b g'_s}{v} \cos \theta \left\{ \left( \frac{c_s h_1 + b_2}{c_s l} + 1 \right), & l < \xi, \\ \frac{c_s h_1 + b_2 + c_s l}{(1 - K)c_s \xi + Kc_s l}, & l \geq \xi, \right. & 0 \leq x < x_{N_b}, \\ 0, & x_{N_b} \leq x \leq x_{N_d}, \end{cases} \tag{B7}$$

and

$$w_{d2}(x, \tilde{t}) = \begin{cases} 0, & 0 \leq x < x_{N_b}, \\ \frac{k_b g'_s}{v} \cos \theta \left\{ \left( \frac{h_2}{l} + 1 \right), & l < \xi, \\ \frac{h_2 + l}{(1 - K)\xi + Kl}, & l \geq \xi, \right. & x_{N_b} \leq x \leq x_{N_d}. \end{cases} \tag{B8}$$

Reassuringly, (B7) and (B8) are consistent with (A7) and (A8) when  $l < \xi$  such that fluid has not yet drained through the depth of the interbed layer.

REFERENCES

- ACTON, D.M., HUPPERT, H.E. & WORSTER, M.G. 2001 Two-dimensional viscous gravity currents flowing over a deep porous medium. *J. Fluid Mech.* **440**, 359–380.
- AJAYI, T., GOMES, J.S. & BERA, A. 2019 A review of CO<sub>2</sub> storage in geological formations emphasizing modeling, monitoring and capacity estimation approaches. *Petrol. Sci.* **16**, 1028–1063.
- ALI, M., JHA, N.K., PAL, N., KESHAVARZ, A., HOTEIT, H. & SARMAVALEH, M. 2022 Recent advances in carbon dioxide geological storage, experimental procedures, influencing parameters, and future outlook. *Earth Sci. Rev.* **225**, 103895.
- ANDERSON, D.M., MCLAUGHLIN, R.M. & MILLER, C.T. 2003 On gravity currents in heterogeneous porous media. *Dev. Water Sci.* **55**, 2810–2829.
- BEAR, J. 1972 *Dynamics of Fluid in Porous Media*. Dover.
- BEHNAM, G.P., BICKLE, M.J. & NEUFELD, J.A. 2021 Two-phase gravity currents in layered porous media. *J. Fluid Mech.* **922**, A7.
- BHARATH, K.S. & FLYNN, M.R. 2021 Buoyant convection in heterogeneous porous media with an inclined permeability jump: an experimental investigation of filling box-type flows. *J. Fluid Mech.* **924**, A35.
- BHARATH, K.S., SAHU, C.K. & FLYNN, M.R. 2020 Isolated buoyant convection in a two-layered porous medium with an inclined permeability jump. *J. Fluid Mech.* **902**, A22.
- COSTALL, A.R., HARRIS, B.D., TEO, B., SCHAA, R., WAGNER, F.M. & PIGOIS, J.P. 2020 Groundwater throughflow and seawater intrusion in high quality coastal aquifers. *Sci. Rep.* **10**, 9866.
- DELGADO, J.M.P.Q. 2007 Longitudinal and transverse dispersion in porous media. *Chem. Engng. Des.* **85**, 1245–1252.
- ELLISON, T.H. & TURNER, J.S. 1959 Turbulent entrainment in stratified flows. *J. Fluid Mech.* **6**, 423–448.
- FARCAS, A. & WOODS, A.W. 2009 The effect of drainage on the capillary retention of CO<sub>2</sub> in a layered permeable rock. *J. Fluid Mech.* **618**, 349–359.
- FELDMANN, F., HAGEMANN, B., GANZER, L. & PANFILOV, M. 2016 Numerical simulation of hydrodynamic and gas mixing processes in underground hydrogen storages. *Environ. Earth Sci.* **75**, 1165.
- GILMORE, K.E., SAHU, C.K., BENHAM, G.P., NEUFELD, J.A. & BICKLE, M.J. 2021 Leakage dynamics of fault zones: experimental and analytical study with application to CO<sub>2</sub> storage. *J. Fluid Mech.* **931**, A31.
- GODA, T. & SATO, K. 2011 Gravity currents of carbon dioxide with residual gas trapping in a two-layered porous medium. *J. Fluid Mech.* **673**, 60–79.
- HASSANPOURYOUBAND, A., JOONAKI, E., EDLMANN, K., HEINEMANN, N. & YANG, J. 2020 Thermodynamic and transport properties of hydrogen containing streams. *Sci. Data* **7** (1), 222.
- HESSE, M.A., TCHELEPI, H.A., CANTWEL, B.J. & ORR, F.M. JR 2007 Gravity currents in horizontal porous layers: transition from early to late self-similarity. *J. Fluid Mech.* **577**, 363–383.
- HUPPERT, H. & WOODS, A.W. 1995 Gravity driven flows in porous layers. *J. Fluid Mech.* **292**, 55–69.
- HUPPERT, H.E., NEUFELD, J.A. & STRANDKVIST, C. 2013 The competition between gravity and flow focusing in two-layered porous media. *J. Fluid Mech.* **720**, 5–14.
- HUYAKORN, P.S., ANDERSEN, P.F., MERCER, J.W. & WHITE, H.O. JR 1987 Saltwater intrusion in aquifers: development and testing of a three-dimensional finite element model. *Water Resour. Res.* **23**, 293–312.
- KHAN, M.I., BHARATH, K.S. & FLYNN, M.R. 2022 Effect of buoyant convection on the spreading and draining of porous media gravity currents along a permeability jump. *Transp. Porous Media* **146**, 721–740.
- LEAHY, M.J., ENNIS-KING, J., HAMMOND, J., HUPPERT, H.E. & NEUFELD, J.A. 2009 Application of gravity currents to the migration of CO<sub>2</sub> in heterogeneous saline formations. *Energy Proced.* **1**, 3331–3338.
- LUBON, K. & TARKOWSKI, R. 2021 Numerical simulation of hydrogen injection and withdrawal to and from a deep aquifer in NW Poland. *ACS Energy Lett.* **6**, 2181–2186.
- MACMINN, C.W., NEUFELD, J.A., HESSE, M.A. & HUPPERT, H.E. 2012 Spreading and convective dissolution of carbon dioxide in vertically confined, horizontal aquifers. *Water Resour. Res.* **48**, 1–21.
- MUHAMMED, N.S., HAQ, M.B., AL-SHEHRI, D.A., AL-AHMED, A., RAHMAN, M.M., ZAMAN, E. & IGLAUER, S. 2023 Hydrogen storage in depleted gas reservoirs: a comprehensive review. *Fuel* **337**, 127032.
- NEUFELD, J.A., HESSE, M.A., RIAZ, A., HALLWORTH, M.A., TCHELEPI, M.A. & HUPPERT, H.E. 2010 Convective dissolution of carbon dioxide in saline aquifers. *Geophys. Res. Lett.* **37**, 1–5.
- NEUFELD, J.A. & HUPPERT, H.E. 2009 Modelling carbon dioxide sequestration in layered strata. *J. Fluid Mech.* **625**, 353–370.
- PASTER, A. & DAGAN, G. 2007 Mixing at the interface between two fluids in porous media: a boundary-layer solution. *J. Fluid Mech.* **584**, 455–472.

- PEGLER, S.S., HUPPERT, H.E. & NEUFELD, J.A. 2014 Fluid injection into a confined porous layer. *J. Fluid Mech.* **745**, 592–620.
- PRITCHARD, D., WOODS, A.W. & HOGG, A.J. 2001 On the slow draining of a gravity current moving through a layered permeable medium. *J. Fluid Mech.* **444**, 23–47.
- VAN REEUWIJK, M., HOLZNER, M. & CAULFIELD, C.P. 2019 Mixing and entrainment are suppressed in inclined gravity currents. *J. Fluid Mech.* **873**, 786–815.
- SAHU, C.K. & FLYNN, M.R. 2015 Filling box flows in porous media. *J. Fluid Mech.* **782**, 455–478.
- SAHU, C.K. & FLYNN, M.R. 2017 The effect of sudden permeability changes in porous media filling box flows. *Transp. Porous Media* **119**, 95–118.
- SAHU, C.K. & NEUFELD, J.A. 2020 Dispersive entrainment into gravity currents in porous media. *J. Fluid Mech.* **886**, A5.
- SAHU, C.K. & NEUFELD, J.A. 2023 Experimental insights into gravity-driven flows and mixing in layered porous media. *J. Fluid Mech.* **956**, A27.
- SHEIKHI, S., SAHU, C.K. & FLYNN, M.R. 2023 Dispersion effects in porous media gravity currents experiencing local drainage. *J. Fluid Mech.* **975**, A18.
- SZULCZEWSKI, M.L. & JUANES, R. 2013 The evolution of miscible gravity currents in horizontal porous layers. *J. Fluid Mech.* **719**, 82–96.
- TARKOWSKI, R. 2019 Underground hydrogen storage: characteristics and prospects. *Renew. Sustain. Energy Rev.* **105**, 86–94.
- THOMAS, L.P., MARINO, B.M. & LINDEN, P.F. 1998 Gravity currents over porous substrates. *J. Fluid Mech.* **366**, 239–258.
- WARNECKI, M., WOJNICKI, M., KUSNIERCZYK, J. & SZUFLITA, S. 2021 Study of the long term acid gas sequestration process in the Borzecin structure: measurements insight. *Energies* **14** (17), 5301.
- WERNER, A.D., BAKKER, M., POST, V.E.A., VANDENBOHEDE, A., LU, C., ATAIE-ASHTIANI, B., SIMMONS, C.T. & BARRY, D.A. 2013 Seawater intrusion processes, investigation and management: recent advances and future challenges. *Adv. Water Resour.* **51**, 3–26.
- ZHENG, Z., GUO, B., CHRISTOV, I.C., CELIA, M.A. & STONE, H.A. 2015 Flow regimes for fluid injection into a confined porous medium. *J. Fluid Mech.* **767**, 881–909.